Disorder-mediated ionic conductivity in irreducible solid electrolytes

Victor Landgraf, Mengfu Tu, Wenxuan Zhao, Anastasia K. Lavrinenko, Zhu Cheng, Jef Canals,

Joris de Leeuw, Swapna Ganapathy, Alexandros Vasileiadis, Marnix Wagemaker[*], Theodosios

Famprikis[*]

Faculty of Applied Sciences, Delft University of Technology, 2629 JB Delft, The Netherlands

Abstract

Solid-state batteries currently receive extensive attention due to their potential to outperform lithium-ion batteries in terms of energy density when featuring next-generation anodes such as lithium metal or silicon. However, most highly conducting solid electrolytes decompose at the low operating voltages of next-generation anodes leading to irreversible lithium loss and increased cell resistance. Such performance losses may be prevented by designing electrolytes which are thermodynamically stable at low operating voltages (anolytes). Here, we report on the discovery a new family of *irreducible* (i.e. *fully reduced*) electrolytes by mechanochemically dissolving lithium nitride into the Li_2S antifluorite structure, yielding highly conducting crystalline $Li_{2+x}S_{1-x}N_x$ phases reaching > 0.2 mS cm^{-1} at ambient temperatures. Combining impedance spectroscopy experiments and *ab initio* density functional theory calculations we clarify the mechanism by which the disordering of the sulfide and nitride ions in the anion sublattice boosts ionic conductivity in $Li_{2+x}S_{1-x}N_x$ phases by a factor 10^5 compared to the Li_2S host structure. This advance is achieved through a novel theoretical framework, leveraging percolation analysis with local-environment-specific activation energies and is widely applicable to disordered ion conductors. The same methodology allows us to rationalize how increasing nitrogen content in $Li_{2+x}S_{1-x}N_x$ antifluorite-like samples leads to both increased ionic conductivity and lower conductivity-activation energy. These findings pave the way to understanding disordered solid electrolytes and eliminating decomposition-induced performance losses on the anode side in solid-state batteries.

Introduction

Solid-state batteries (SSBs) are recently receiving considerable attention in the scientific community because of their potential to outperform conventional lithium-ion batteries.[1,2] The potential advantages of SSBs originate from their solid nature and single-ion conductivity, improved safety and the possibility of efficient cell stacking (*bipolar stacking*).[1] SSBs will likely only overcome conventional lithium-ion batteries in terms of energy density, if they feature low-potential, high-energy-density anodes such as Si (ref.[3]) or Li-metal anodes.[4,5] Most highly-conducting solid electrolytes decompose at the low potentials of Si and Li metal anodes.[6–8] The decomposition into solid electrolyte interphase (SEI) entails irreversible Li-loss – particularly an issue for industrially attractive *zero-Li-excess* battery cells.[9] Irreversible Li loss from SEI formation may be mediated in three ways: (i) by limiting the contact area between the solid-electrolyte and anode[10,11], (ii) by adding sacrificial Li agents such as for instance Li_3N to the cathode [12,13] or (iii) by designing solid electrolytes which are thermodynamically stable at the operating potentials of low-potential anodes.

Irreducible or *fully reduced* phases are thermodynamically stable against Li metal and are thus inherently irreducible against low-potential anodes. *Irreducible* refers to all elements (except for Li) in the material being in their lowest possible formal oxidation state (i.e. *fully reduced)* and thus not further reducible. Examples of irreducible phases are lithium binaries (e.g. Li_2S, $LiCl$, $LiBr$, Li_2O, Li_3N), lithium-rich antiperovskites (e.g. Li_3OCl, Li_3OBr; see refs.[14,15]), Li_5NCl_2 (refs.[16,17]) and the recently discovered $Li_{2+x}S_{1-x}P_x$ ($0<x<0.75$) solid solution.[18] An issue with irreducible phases thus far has been that their ambient-temperature conductivities do not typically reach values above 0.05 mS cm^{-1} —Li_3N and $Li_{2.75}S_{0.25}P_{0.75}$ are exceptions with RT conductivities of 0.5 mS cm^{-1} (ref.[19]) and ~0.25 mS cm^{-1} (ref.[18]), respectively. The latter $Li_{2+x}S_{1-x}P_x$ ($0<x<0.75$) solid solution [18] is characterized by a disordered anion lattice, yet the effect of the structural disorder on ion conductivity has not yet been clarified.

Structural disorder on the atomic scale —often occupational (i.e. characterized by multiple partially occupied cation positions) and/or compositional (i.e. characterized by mixed occupation of framework sites by multiple different atoms)—is in fact a common feature of most highly

2

54 conductive solid electrolytes. Both of these types of disorder feature, for example, in the well-
55 studied argyrodite family of ion conductors with the archetypical formula Li_6PS_5X (X: Cl, Br).
56 Nevertheless, the correlation between disorder and ionic conductivity remains a qualitative one.
57 Zeng et al. argued in a recent study that the (often) enhanced conductivity in compositionally
58 disordered solid electrolytes originates from the increased energy-overlap between individual
59 carrier-ion (Li, Na, ...) sites, enabling low-energy percolation paths through solid-electrolyte
60 crystallites —without explicitly considering the energetics of ion hops but instead based on the
61 assumption that sites similar in energy are connected by low activation barriers.[20]

62 In the present study, we report the discovery of a new family of irreducible solid electrolytes
63 with the general formula $Li_{2+x}S_{1-x}N_x$ (0<x<0.55) reaching high conductivities above 0.2 mS cm^{-1}.
64 These are metastable phases, accessible by mechanochemistry and feature a disordered
65 face-centered-cubic arrangement of nitride and sulfide anions. We further develop a widely
66 applicable methodology to investigate the effect of disorder on conductivity that explains the
67 often observed conductivity increase with increased structural disorder. The herein developed
68 methodology comprises the analysis of ion-hop activation energies from molecular dynamics
69 (MD) as a function of local environments and their connectivity via percolation analysis.

70 We leverage this MD-percolation methodology to rationalize the conductivity boost in the
71 disordered $Li_{2+x}S_{1-x}N_x$ phases. We find that the disordered N/S anion arrangement in $Li_{2+x}S_{1-x}N_x$
72 electrolytes is causally related to their vastly increased ionic conductivity compared to the
73 structurally and chemically related anion-ordered Li_2S and Li_9S_3N (refs. [21,22]), by allowing low-
74 activation-energy ion jumps through locally nitrogen-rich bottlenecks. We show how the MD-
75 percolation methodology may be applied to other disordered solid electrolytes which we
76 demonstrate on the example of the Li_6PS_5Br argyrodite.

Results and Discussion

Synthesis of disordered-Li_9S_3N

79 Previous investigations on the Li_2S-Li_3N tieline identified the anion-ordered Li_9S_3N phase
80 accessible by conventional solid-state synthesis[21,22]. After reproducing said synthesis (SI Figure
81 S1, Table S1), we attempted to synthesize Li_9S_3N mechanochemically, through milling

3

82　stoichiometric amounts of the precursors (Li_2S and Li_3N). The x-ray and neutron diffraction

83　patterns of the resulting product did not show any leftover precursors (Figure 1, Figure S1) and

84　we verified through diffraction that no significant amorphous fraction or amorphous impurities

85　are present in samples synthesized with this approach (see Supplementary Note 1).
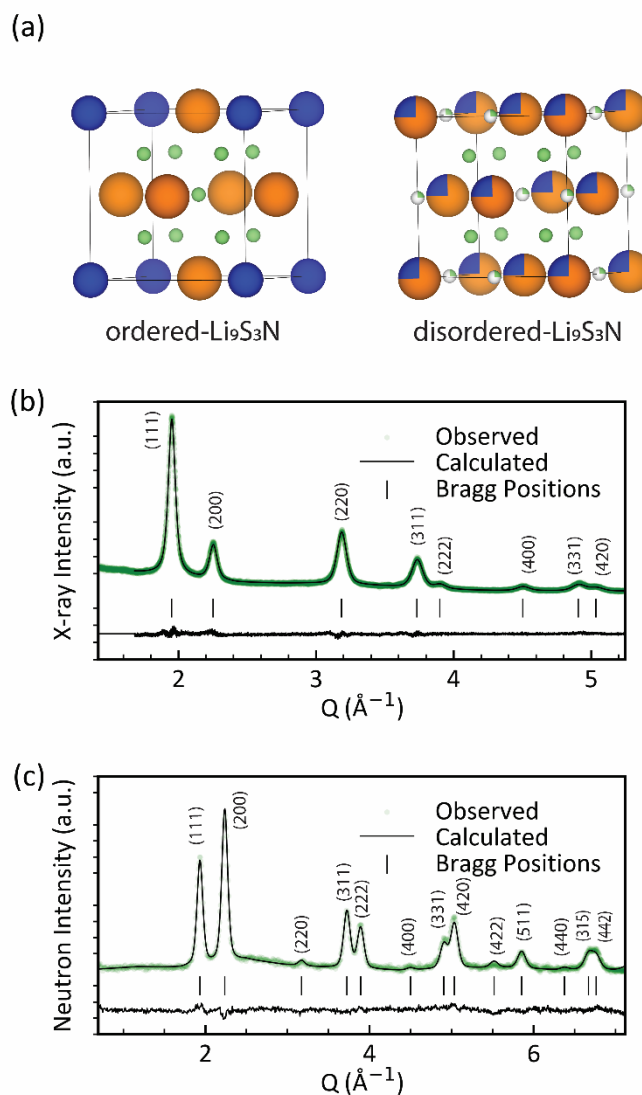
86

Figure 1. Neutron and x-ray powder diffraction on mechanochemically-synthesized anion-disordered Li_9S_3N. (a) Unit cell of anion-ordered ($Pm\overline{3}m$) and anion-disordered ($Fm\overline{3}m$) Li_9S_3N. (b) x-ray- and (c) neutron diffraction patterns of mechanochemically-synthesized anion-disordered Li_9S_3N along with Rietveld refinements.

4

87 Interestingly, poor Rietveld refinements were obtained when attempting to fit the same $Pm\overline{3}m$-

88 Li$_9$S$_3$N structure solution proposed by Marx et al. [21] to the neutron and x-ray diffraction patterns

89 of the mechanochemically prepared product (SI Figure S2). The $Pm\overline{3}m$-Li$_9$S$_3$N structure solution

90 proposed by Marx et al. [21] (inset Figure 1a, Table S1) is closely related to the antifluorite ($Fm\overline{3}m$)

91 structure of Li$_2$S but the face-centered symmetry is broken by the ordered arrangement of sulfur

92 and nitrogen and an additional Li yielding a unit cell with a lower-symmetry $Pm\overline{3}m$ space group

93 and more non-zero-intensity diffraction peaks.

94 The absence of certain diffraction peaks in the measured diffraction pattern of

95 mechanochemically synthesized Li$_9$S$_3$N suggests that the crystal structure of mechanochemically

96 prepared Li$_9$S$_3$N has a higher symmetry than the $Pm\overline{3}m$ structure that Marx et al.[21] proposed for

97 ampoule-synthesized Li$_9$S$_3$N. The increased symmetry may originate from a mechanochemically-

98 induced disordering of the S and N atoms. Inspired by the crystal structure of the cubic lithium-

99 deficient antifluorite lithium-nitride-halide Li$_5$NCl$_2$ (ref. [16]), we propose the following structure

100 for mechanochemically-prepared Li$_9$S$_3$N (SI Table S2) : Cubic $Fm\overline{3}m$ with S and N sharing

101 occupation of the Wyckoff 4a (0,0,0) position in a 3:1 proportion as imposed by the Li$_9$S$_3$N

102 stoichiometry. The tetrahedral interstitial on the Wyckoff 8c (0.25, 0.25, 0.25) position is fully

103 occupied by Li and the octahedral interstitial on the Wyckoff 4b (0.5, 0.5, 0.5) position is partially

104 occupied (25 %) by Li (Figure 1a). In that sense the structure can be considered as an intermediate

105 between the antifluorite (only tetrahedral sites fully occupied; e.g. Na$_2$O, Li$_2$S) and Li$_3$Bi (both

106 tetrahedral and octahedral sites fully occupied) archetypical structures based on interstitial-filling

107 of face-centered lattices.

108 The proposed lithium-rich disordered antifluorite ($Fm\overline{3}m$) structure solution is supported by the

109 much improved neutron and x-ray Rietveld refinements (SI Figure S3). We thus discovered a new

110 material which can be interpreted as a disordered polymorph of the previously known $Pm\overline{3}m$

111 phase[21]. Based on our structure solution we will from now on refer to the mechanochemically

112 synthesized, anion-disordered ($Fm\overline{3}m$) Li$_9$S$_3$N as *disordered*-Li$_9$S$_3$N and to

113 solid-state-synthesized, anion-ordered ($Pm\overline{3}m$) Li$_9$S$_3$N as *ordered*-Li$_9$S$_3$N.

5

114   We note that the structure solution we propose for disordered-Li_9S_3N (Figure 1a, Table S2)

115   features large thermal parameters on the Li-sites ($U_{iso} > 0.07$ Å^2). An in-depth structure analysis

116   supported by molecular dynamics simulations (Supplementary Note 2) demonstrates that these

117   large U_{iso} values originate from displacive relaxations of lithium ions off their ideal positions

118   correlated to the specific local N/S coordination. We also propose an alternative structure

119   solution, in which the octahedral lithium positions are further resolved via site-splitting in

120   combination with lower U_{iso} values. Still, the simple structure solution presented in Figure 1a and

121   Table S2 captures all the essential features to describe the disordered-Li_9S_3N phase for all

122   following discussions.

123   **Effect of S/N disordering on the conductivity in disordered-Li_9S_3N**

124   To compare the ionic conductivities of ordered- and the newly discovered disordered-Li_9S_3N we

125   performed variable-temperature impedance spectroscopy experiments on pelletized powder

126   samples (Figure 2). Interestingly, we found an activation energy reduced by 80 meV and a

127   significant ambient-temperature conductivity increase by a factor 30 for disordered-Li_9S_3N (0.064

128   mS cm^{-1}), compared to ordered-Li_9S_3N (0.0018 mS cm^{-1}). Next, we occupy ourselves with the

129   underlying mechanism that enabled the 30-fold conductivity increase and the reduced activation

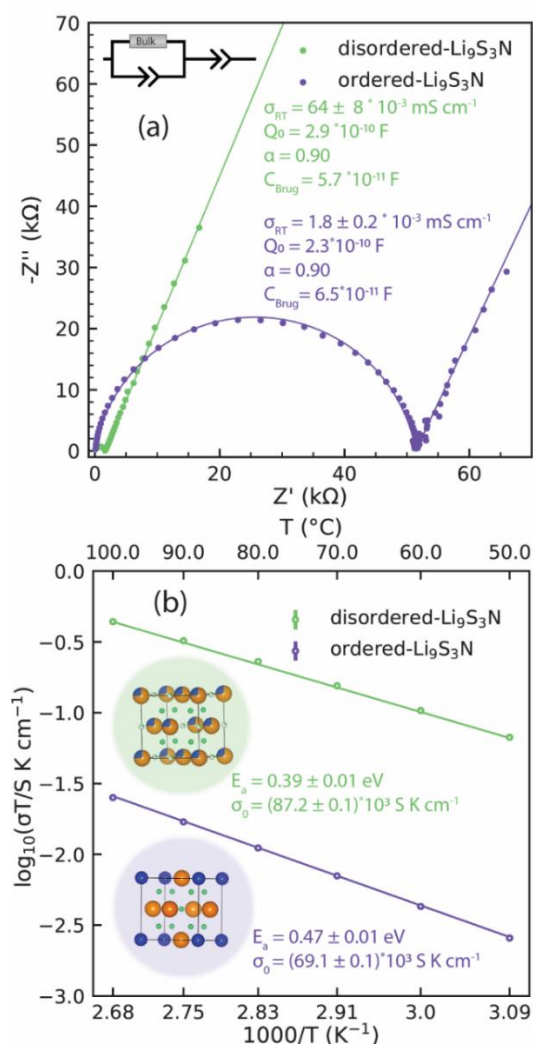130   energy in disordered-Li_9S_3N compared to ordered-Li_9S_3N.

Figure 2. Impedance spectroscopy results for ordered and disordered-Li_9S_3N. (a) Room-temperature impedance spectra fitted with the equivalent circuit inset. (b) The Arrhenius plots and fits. All data points obtained from at least two measurements. Error bars often smaller than marker symbol. Inset: structural models with Li, S, N in green, orange, blue, respectively.

131   Ordered- and disordered-Li_9S_3N feature the same face-centered-cubic anion framework and the

132   same lithium (and thus, vacancy) content and so the change in conductivity cannot be ascribed

133   to the overall concentration of charge carriers. Thus we hypothesize that the vastly different ionic

134   conductivity observed in Figure 2 should originate in changes to the relative mobility of Li^+ ions

135   as a function of the different local structure. To probe this hypothesis we initiated a series of *ab*

136   *initio* molecular dynamics (AIMD) simulations with ordered-Li_9S_3N and disordered-Li_9S_3N

137   supercells. In disordered supercells the Wyckoff 4a position was randomly decorated with N and

7

138 S, respecting the 1:3 ratio imposed by the Li_9S_3N stoichiometry. The Wyckoff 4b position was also

139 randomly decorated with Li atoms and vacancies respecting the overall stoichiometry. As done

140 in previous studies we dissected our AIMD simulations into individual jump events. [16,23–26] In-

141 depth analysis of the AIMD simulations shows that well-defined sites exist in (dis)ordered Li_9S_3N

142 and that jumps between these sites occur mostly independently (i.e. *no* evidence of correlated

143 ion jumps, correlated "cascades" of jumps or correlated "strings" of jumps is found which have

144 been reported in other high-conducting solid electrolytes such as Li_6PS_5Cl (ref.[27]) and $Li_{10}GeP_2S_{12}$

145 (ref.[28]) , see Supplementary Note 5).

146 From the frequency of jumps between two sites ($v_{A\text{-}>B}$) we calculate so-called jump-activation

147 energies (jump-Ea) by using equation (1):

$$jump\ E_{a,A\to B} = -k_b T \cdot \ln\left(\frac{v_{A\to B}}{v_0}\right) \quad (1)$$

149 where jump-$E_{a,\ A\text{-}>B}$ the jump-activation energy of a jump event from site A to site B, k_b the

150 Boltzmann constant, T the temperature in K, $v_{A\text{-}>B}$ the observed frequency of jumps between sites

151 A and B and v_0 the *attempt* frequency, which we assume to be 10^{13} Hz. The latter is a widely

152 accepted approximation for ceramic ion conductors[29–32] and we additionally verified that this

153 approximation applies for the Li_9S_3N system (see Supplementary Note 4).

154 The jump-$Ea_{A\text{-}>B}$ is a rescaled jump frequency that we interpret as a proxy for the time-averaged

155 local ion hop activation energies and thus the ease of the ion jump from site A to site B. We note

156 that, while both quantify the ease of migration, energy barriers obtained from nudged-elastic-

157 band calculations and the jump-Ea values from AIMD used here are conceptually different and

158 not necessarily equivalent as explained in Supplementary Note 5.

159 Adopting the above described approach, we could assign an individual jump-Ea values to each

160 different jump type based on local coordination and bottleneck composition. Irrespective of local

161 anion ordering, three general families of jumps are observed through the face-centered anion

162 arrangement in Li_9S_3N. (i) tetrahedron(*8c*)-to-octahedron(*4b*) (tet-oct), (ii) octahedron(*4b*)-to-

163 tetrahedron(*8c*) (oct-tet) and (iii) tetrahedron(*8c*)-to-tetrahedron(*8c*) (tet-tet) jumps.

164 Tetrahedral sites are connected to adjacent octahedral sites via triangular bottlenecks composed

8

165   of three anions, whereas two tetrahedral sites are connected through linear bottlenecks

166   composed of two anions. Both, triangular and linear bottlenecks are shown schematically in

167   Figure 3 for ordered- and disordered-Li_9S_3N.

168   We characterize a jump event by its start-site, its end-site and the bottleneck connecting the two

169   sites and use a *start-end(bottleneck)* notation. For example, a S_3N-S_6(SSS) jump is a tet-oct jump

170   which starts at a tetrahedral-Li site where the corners of the tetrahedron are occupied by three

171   sulfide and one nitride ion for which we use the notation S_3N_1. From there on the jump path

172   proceeds through a triangular bottleneck consisting of three sulfide ions for which we use the

173   notation SSS. The end-point of this jump is an octahedral Li site where the corners of the

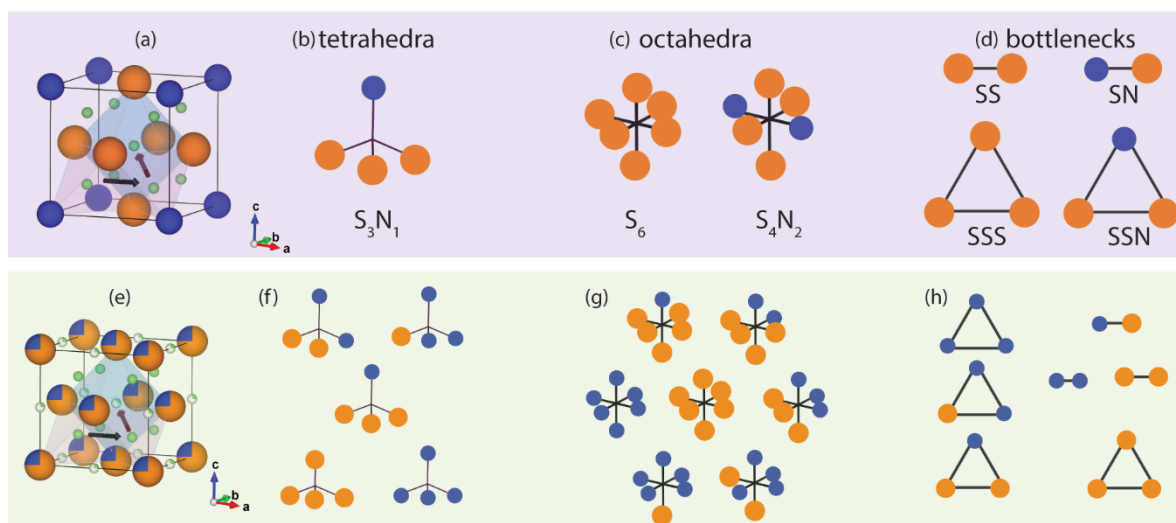174   octahedron are all occupied by sulfide ions for which we use the notation S_6.

Figure 3. Local environments in ordered- and disordered-Li_9S_3N . (a) unit cell of ordered-Li_9S_3N (**$Pm\overline{3}m$**). Example, tetrahedral and octahedral lithium positions in pink and blue, respectively. Black arrows indicate tet-tet and oct-tet jump paths. (b) single tetrahedral site, S_3N_1 present in ordered-Li_9S_3N. (c) Two octahedral sites present in ordered-Li_9S_3N: S_6 and S_4N_2. (d) Two linear bottlenecks (SS, NS) and two triangular bottlenecks (SSS, SSN) present in ordered-Li_9S_3N. (e) unit cell of disordered-Li_9S_3N (**$Fm\overline{3}m$**). (f) All five possible tetrahedral compositions in disordered-Li_9S_3N. (g) all seven possible octahedral coordinations in disordered-Li_9S_3N. (h) all three linear and four triangular bottlenecks possible in disordered-Li_9S_3N. Li, S, N in green, orange, blue, respectively.

175   Figures 3a and 3e schematically illustrate the tet-tet and oct-tet jump paths through the linear

176   and triangular bottlenecks for the crystal structure of ordered-Li_9S_3N and disordered-Li_9S_3N,

177   respectively. Figure 3 shows that the disorderly arrangement of S/N in disordered-Li_9S_3N enables

9

178   a large manifold of different jump types (91 jump-types, Table S3), as a result of the possible

179   permutations between starting site, ending site and bottleneck compositions. For instance,

180   taking the example of triangular bottlenecks, in disordered-Li_9S_3N, SSS, NSS, NNS and NNN

181   bottlenecks may exist whereas in ordered-Li_9S_3N only SSS and NSS bottlenecks exist (Figure 3d,h).

182   To enable high conductivity, SEs should feature low-energy percolating paths consisting of a

183   series of connected Li jumps with low jump-activation energies. Figure 4a demonstrates the

184   jump-Ea values of individual jump types segregated by local environment and determined by

185   equation (1) from the MD trajectories. Because of its ordered S/N arrangement, ordered-Li_9S_3N

186   merely features 6 discrete jumps which are shown as discreet points in Figure 4a. The uncertainty

187   on individual jump-Ea values is in the range of 10-30 meV and comprises uncertainty associated

188   to convergence as further explored in Supplementary Note 6. The tet-oct jumps being generally

189   higher in energy than the oct-tet jumps is coherent with the fact that the octahedral sites are

190   generally higher in energy compared to the tetrahedral ones (Figure S4), which in turn is coherent

191   in the crystallographic model of full tetrahedral- and only partial octahedral Li occupation.

192   In both phases, ordered- and disordered-Li_9S_3N, long-range bulk diffusion occurs along *tet-oct-*

193   *tet* or *tet-tet* diffusion paths. To illustrate the effect of the determined jump-Ea values on Li

194   diffusion we take the example of a jump-Ea threshold of 0.4 eV: Ordered-Li_9S_3N does not feature

195   tet-oct or tet-tet jumps with a jump-Ea < 0.4 eV. Thus *oct-tet-oct* or *tet-tet-tet* diffusion paths —

196   necessary for percolation— where each individual jump has a jump-Ea < 0.4 eV cannot exist and

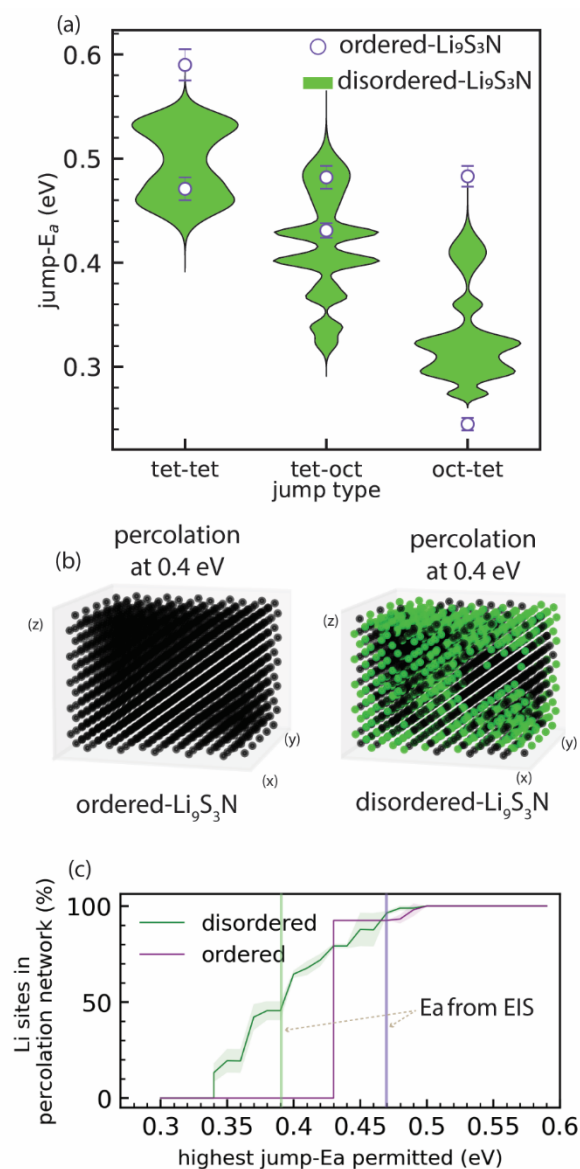197   thus no percolation is possible with an overall activation-energy threshold < 0.4 eV.

10

Figure 4. Effect of different jump-types existing in ordered and disordered Li_9S_3N. (a) Comparison of the observable jump-activation energies in ordered and disordered-Li_9S_3N. Purple markers indicate jump-Ea of six distinct jump types possible in ordered-Li_9S_3N, labelled with the *start-end(bottleneck)* notation explained in the main text. In disordered-Li_9S_3N 91 different jumps are observable, listed in SI Table S8 and shown here as density plots (*violins*). The horizontal scale of the violins represent the relative occurrence of jump types at that energy. (b) Lattice of 1500 lithium sites for ordered and disordered Li_9S_3N (5x5x5) supercells. Sites highlighted in green are part of percolating networks with an energy threshold ≤0.4 eV. (c) Percolation-energy diagram showing the fraction of Li sites that are connected to percolating networks (averaged over 50 disordered 5x5x5 supercells) for ordered- and disordered-Li_9S_3N. Shading is the standard deviation over 50 supercells. The vertical lines indicate the experimental activation energy $E_{a,EIS}$ obtained experimentally from EIS for ordered- and disordered-Li_9S_3N (see Figure 2).

11

198   In contrast to ordered-Li_9S_3N, the disordering of S/N in disordered-Li_9S_3N enables a large manifold

199   of 91 different jump types, of which the distribution of jump-activation energies are shown in

200   Figure 4 as density (*violin*) plots. In contrast to the ordered case, the disordering of anions creates

201   tet-oct and tet-tet jumps with jump-Ea's < 0.4 eV. Thus *oct-tet-oct* and *tet-tet* diffusion paths

202   where each individual jump has a jump-Ea < 0.4 eV are conceivable —and thus percolation with

203   an overall activation-energy threshold <0.4 eV is possible. From a comparison of the same jump

204   types in ordered and disordered Li_9S_3N supercells it becomes apparent that the long-range anion

205   ordering in ordered-Li_9S_3N has a Li-diffusion hampering effect in addition to the local N/S

206   occupation of polyhedra and bottlenecks as further explored in Supplementary Note 7.

207   In summary, the above analysis presented in Figures 3 and 4 suggests that the improved

208   conductivity of disordered-Li_9S_3N originates from the disorder-induced numerous possibilities of

209   octahedral and tetrahedral local coordination environments which introduce new jump-types

210   with low jump-activation energies which enable lower-energy percolating paths that cannot exist

211   in the ordered case.

212   To consolidate the hypothesis that percolating lower-energy diffusion paths exist in disordered-

213   Li_9S_3N we designed a percolation model. In this percolation model, 5x5x5 supercells are

214   considered, containing 125 formula units of Li_9S_3N, and 1500 lithium sites (Figure 4b). Each Li site

215   is related to its neighbors based on the jump-activation energies determined previously. A

216   connection is made between two Li sites if the jump-Ea for both the forward and the backward

217   jump are below a defined jump-Ea cutoff value. If —for a defined jump-Ea cutoff value— a

218   connected path can be found spanning the supercell, then the path is *percolating*, provided that

219   the end-point of percolation is itself a starting-point of a percolating path (as illustrated in Figure

220   S5).

221   The results of our percolation analysis are demonstrated in Figures 4b and 4c. Figure 4b shows

222   that for ordered-Li_9S_3N no percolating path exists when the jump-Ea cutoff is set to 0.4 eV. In

223   contrast, for a disordered-Li_9S_3N supercell with the same jump-Ea cutoff of 0.4 eV a clear

224   percolating network is obtained. Our model also determines the number of Li sites that are

225   connected to the percolating network. As the example in Figure 4b demonstrates, even if a

12

226   percolating network exists, a fraction of Li sites may still be disconnected which may lead to a

227   fraction of Li sites which do not (or significantly more slowly) participate in Li-ion diffusion than

228   Li sites in the percolating network. Li sites in disordered-Li_9S_3N may thus be segregated in *active*

229   and *inactive* sites with regards to long-range lithium diffusion[*]. In other words, the majority of

230   jump events involves only a subset of sites that predominantly contribute to the diffusivity

231   (*active*) while the rest remain invariantly vacant or occupied throughout much of the simulation

232   (*inactive*); as may be directly observed from the frequency of occupation change in our AIMD

233   simulations (Figure S6).

234   Figure 4c is a percolation-energy diagram and shows the fraction of Li sites in percolating

235   networks for ordered-Li_9S_3N and disordered-Li_9S_3N (average of 50, 5x5x5 supercells) as a function

236   the highest jump-Ea value allowed in the percolation network. The onset of percolation —that is

237   the lowest activation energy for which a percolation network can exist— is markedly lower in the

238   disordered case (0.34 eV) compared to the ordered case (0.43 eV). This is a direct reflection of

239   the lower energy tet-tet and tet-oct jumps available in the disordered case shown in Figure 4a

240   but additionally highlights that their connectivity is sufficiently likely to enable percolation paths

241   at lower energy thresholds. The lower energy of percolation onset of disordered-Li_9S_3N suggests

242   that long-range diffusion can be sustained more easily in disordered-Li_9S_3N than in ordered-

243   Li_9S_3N. The presence of diffusion at lower energy thresholds is indeed experimentally reflected

244   in the lower activation energy of disordered- Li_9S_3N (0.39 eV) compared to ordered- Li_9S_3N (0.47

245   eV, Figure 2b). In both cases the conductivity-activation energy is 0.04-0.05 eV higher than the

246   simulated percolation-onset energy.

247   The fact that the experimental *conductivity-activation* energy values are slightly higher than the

248   simulated *percolation-onset* energy values is consistent with the expectation that percolation

249   networks at higher energies than the percolation onset also contribute to the overall diffusion

250   (see Supplementary Note 8).

---

[*] We note that the 'active' versus 'inactive' nomenclature used here, is conceptually comparable to the 'accessible' and 'inaccessible' nomenclature used in the disordered rock-salt cathode literature [69]

13

251   We conclude at this stage that the increased conductivity of disordered-Li_9S_3N is a consequence

252   of the disordered anionic sublattice which enables numerous octahedral and tetrahedral lithium

253   coordination by combinations of sulfide and nitride ions. Instead of only having S_6, S_4N_2 and N_1S_3

254   polyhedra like in ordered-Li_9S_3N, disordered-Li_9S_3N features a wide manifold of polyhedra (N_2S_2,

255   S_3N_3, S_2N_4, S_3N_1....). The diverse configurations of the polyhedra in disordered-Li_9S_3N create new

256   sites and bottlenecks which are simply not present in ordered-Li_9S_3N. Some among these new

257   sites and low-energy bottlenecks enable lower-energy percolation and thus the increased

258   conductivity in disordered-Li_9S_3N. The presented mechanism for disorder-induced conductivity

259   enhancement and the analysis approach developed here for Li_9S_3N are widely applicable to other

260   solid electrolytes as we demonstrate using the example of the entirely different Li_6PS_5Br

261   argyrodite system in Supplementary Note 9.

262   The presented analysis of local jump environments and percolation also enables to optimize ion

263   diffusion by identifying diffusion-promoting and diffusion-hampering local environments.

264   Subsequently, ion diffusion may be optimized by tuning the phase composition to increase the

265   occurrence of diffusion-promoting environments as presented in the following sections.

266   **Understanding diffusion bottlenecks in disordered-Li_9S_3N**

267   Next we explore the relationship between bottleneck composition and local jump-activation

268   energy in disordered-Li_9S_3N. It is expected that the composition of the bottlenecks affects the

269   bottleneck size through the different sizes of the sulfide and nitride anions. The empty space

270   available for Li^+ in the bottlenecks for different oct-tet ion jumps may be estimated from

271   geometrical considerations by determining the diameter of the circle inscribed in the triangle

272   spanned by the surrounding anions (taking into account their anionic radii) as shown in Figure 5a

273   (Table S5 summarizes the ionic radii used for the following considerations, Figure S7 shows how

274   the bottleneck diameter is analogously obtained for linear bottlenecks between tet-tet jumps).

275   The average bottleneck size and its standard deviation were calculated from 50 DFT-relaxed

276   (2x2x2) disordered Li_9S_3N supercells (>9000 bottlenecks) to account for local distortions which

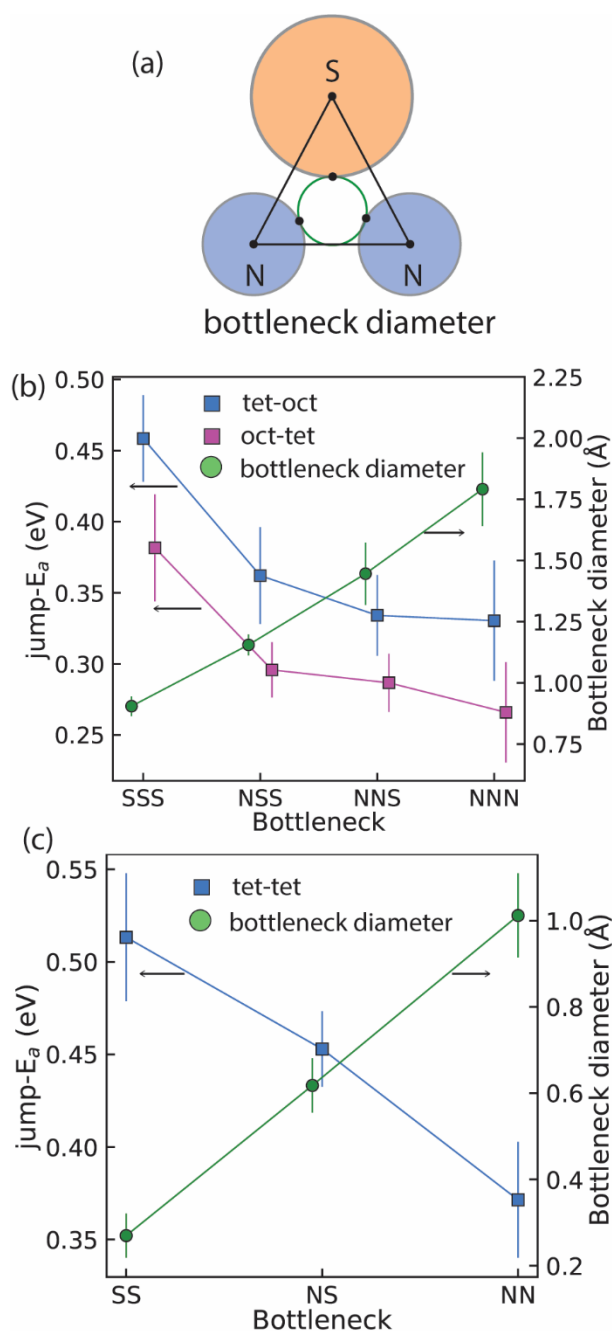277   may not be present in long-range averaged crystallographic unit cells.

14

Figure 5. Relation between jump activation energies and bottleneck sizes in disordered-Li_9S_3N. (a) Illustration of bottleneck definition based on ionic radii of peripheral anions for tet-oct and oct-tet jumps. Analogous definition for tet-tet bottlenecks in Figure S7 (b) Average jump-Ea and bottleneck diameter for tet-oct and oct-tet jumps segregated by bottleneck composition. (c) Average jump-Ea and bottleneck diameter for tet-tet jumps segregated by bottleneck composition. Error bars represent standard deviations from the multiple occurrences of each bottleneck considered.

278　　Figure 5b shows the bottleneck size and average jump-Ea for tet-oct and oct-tet jumps in

279　　disordered-Li_9S_3N as a function of the different possible jump bottlenecks. This analysis shows

15

280　that the more nitrogen the bottleneck contains the larger the bottleneck which can be

281　rationalized based on the small ionic radius of N^{3-} (1.46 Å, ref [33]) compared to S^{2-} (1.84 Å, ref [33]).

282　Further, the more nitrogen a bottleneck contains the lower the jump-Ea. The same trends hold

283　for tet-tet jumps, shown in Figure 5c.

284　We thus observe a correlation between bottleneck size and jump-Ea. In order to rationalize this

285　observation, a useful benchmark is to compare the bottleneck sizes to the diameter of Li^+ at about

286　1.18 Å. As the bottleneck size approaches the size of Li^+, the jump-activation decreases,

287　presumably because of the lessened energy penalty associated with an anion-cation approach

288　smaller than the sum of their ionic radii. This is observed for the tet-tet cases (Figure 5c) and

289　partly for the tet-oct cases (Figure 5b). For the latter, there is a stark effect in going from an SSS

290　bottleneck (diameter: 0.90 Å) to NSS (1.15 Å) resulting in a decrease in jump-Ea of approximately

291　100 meV.

292　As the bottleneck size reaches and surpasses the size of Li^+ —that is, in the case of NSS, NNS and

293　NNN triangular bottlenecks— the effect of bottleneck-diameter widening on decreasing jump-Ea

294　is lessened and the corresponding jump-activation energies plateau. We quantify the amount of

295　time lithium ions are in unfavorable proximity to the anions (defined as closer than the sum of

296　their respective radii) in SI Figure S8, and show indeed that the lower jump-Ea correlates with

297　less time spent too close to the anions.

298　We have thus established that the jump-Ea generally decreases the more nitrogen the bottleneck

299　contains and we thus identified diffusion-promoting local environments. Based on this

300　observation, we hypothesize that introducing more nitrogen into disordered-Li_9S_3N would

301　increase the number of low-energy nitrogen-containing bottlenecks, thus increasing the number

302　of lower-energy percolation paths, in turn leading to more facile ion conduction.

303　**Solid Solution between Li_3N and Li_2S: Lithium-rich disordered antifluorite phases $Li_{2+x}S_{1-x}N_x$**

304　To probe the hypothesis that nitrogen content controls ionic conductivity in the sulfide-nitride

305　antifluorites, we synthetically explored compositions on the tie line between Li_2S and Li_3N. The

306　two Li_9S_3N phases lie on the $(1-x)Li_2S-xLi_3N$ tie line with x=0.25. Our findings so far suggest that

307　nitrogen-richer $Li_{2+x}S_{1-x}N_x$ antifluorite phases –if existing– would likely have even higher

16

308   conductivities than the disordered-Li_9S_3N (i.e. $Li_{2.25}S_{0.75}N_{0.25}$) because of the higher occurrence of

309   low-energy, nitrogen-rich bottlenecks.

310   Figure 6 shows the results of our synthetic exploration of the Li_2S-Li_3N tie line via

311   mechanochemistry. For samples of overall stoichiometry $(1-x)Li_2S$-xLi_3N with $0<x<0.55$, a single

312   ($Fm\overline{3}m$) antifluorite-like phase was observed in the diffractograms (shown in Figure S9),

313   indicating that Li_3N dissolves in the antifluorite structure of Li_2S to form a $Li_{2+x}S_{1-x}N_x$ solid solution

314   of anion-disordered phases illustrated in Figure 6a. Nitrogen-richer $Li_{2+x}S_{1-x}N_x$ phases have

315   expectedly smaller lattice parameters as obtained from refinements of x-ray diffraction patterns
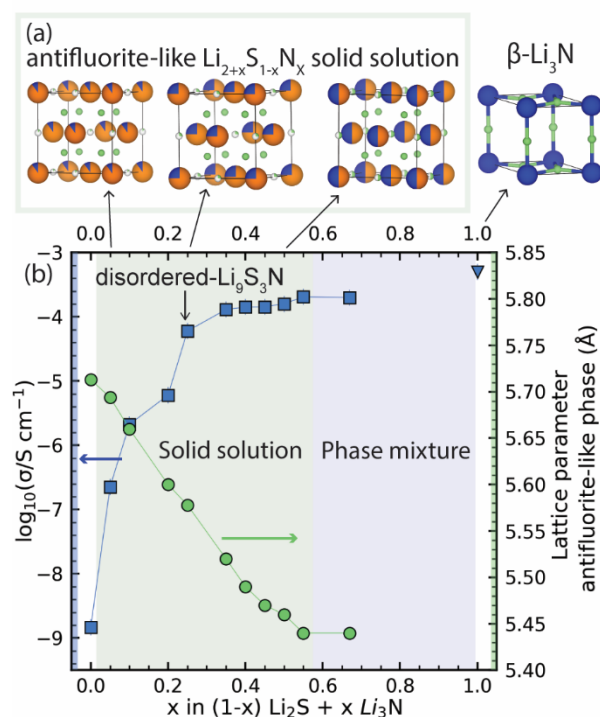
316   and plotted in Figure 6b.

Figure 6. Conductivity of the antilfluorite-like solid solution on the $(1-x)$ Li_2S-x Li_3N tie line $(0<x<0.55)$. (a) Schematic illustration of the $Li_{2+x}S_{1-x}N_x$ $(0<x<0.55)$ solid solution and hexagonal β-Li_3N (b) Ionic conductivity and lattice parameter (of antifluorite-like phase) for $(1-x)$ Li_2S-x Li_3N samples. Green and blue shading indicates antifluorite-like solid solution $(0<x<0.55)$ and phase separation $(0.55<x<1)$ regions, respectively. Lines are guides to the eye.

317   At $x=0.55$ the lattice parameter ceases to decrease with increasing nitrogen content. The

318   diffraction pattern of an attempted synthesis with nominal stoichiometry 0.33 Li_2S-0.67 Li_3N (i.e.

319    $x=0.67$) showed a phase mixture of Li_3N and an antifluorite $Li_{2+x}S_{1-x}N_x$ phase (Figure S9) with the

17

same lattice parameter as $Li_{2.55}S_{0.45}N_{0.55}$ indicating that the solubility limit of Li_3N in Li_2S is reached at $x≈0.55$. The nitrogen-richest phase in the $Li_{2+x}S_{1-x}N_x$ antifluorite solid solution is thus $Li_{2.55}S_{0.45}N_{0.55}$.

Figure 6b shows that the conductivity increases with increasing nitrogen content in antifluorite-like $Li_{2+x}S_{1-x}N_x$ ($0<x<0.55$). For antifluorite Li_2S, mechanochemically milled without Li_3N (i.e. $x=0$), we measured a room-temperature conductivity of 10^{-9} S cm^{-1}. Dissolving a small fraction ($x=0.05$) of nitrogen into the Li_2S host structure already improves the room-temperature conductivity by more than 2 orders of magnitude to $2.2 * 10^{-7}$ S cm^{-1}. The conductivity then steadily increases with increasing nitrogen content reaching a high conductivity of 0.22 mS cm^{-1} near the solubility limit at $x=0.55$. Li_3N can thus be dissolved in Li_2S leading to a series of fully reduced solid electrolytes with high ionic conductivities. The conductivity of $β$-Li_3N (0.5 mS cm^{-1}) is also shown in Figure 6b for comparison —though we note that $β$-Li_3N is structurally unrelated to the antifluorite-like $Li_{2+x}S_{1-x}N_x$ solid solution.

We measured the conductivity-activation energy of several synthesized $Li_{2+x}S_{1-x}N_x$ phases ($x=0.05$, 0.1, 0.2 0.25, 0.45) via impedance spectroscopy at varying temperatures. Figure 7a shows that the experimental activation energy of $Li_{2+x}S_{1-x}N_x$ phases decreases with increasing nitrogen content, suggesting lithium diffusivity at lower energy thresholds. The observation of higher room-temperature conductivity and lower conductivity-activation energy is consistent with our expectation from the analysis of jump-Ea values and their dependence on the bottleneck composition.
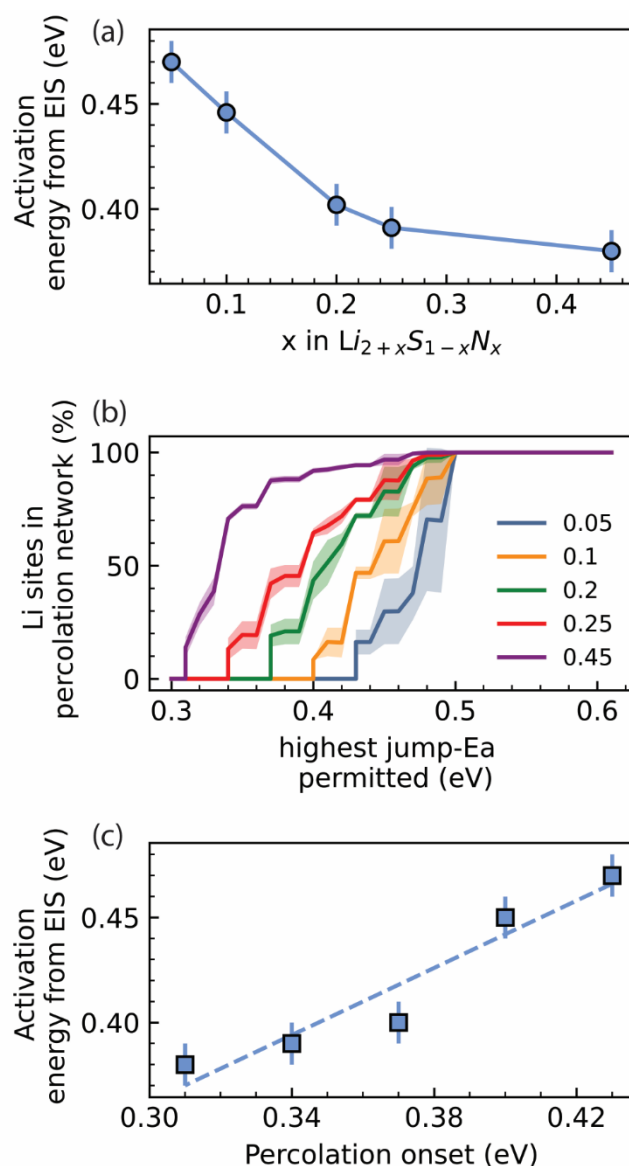
18

Figure 7. Rationalizing the decreasing activation energy for increased nitrogen content in $Li_{2+x}S_{1-x}N_x$ (0<x<0.55) antifluorite-like phases. (a) Activation energy obtained from impedance spectroscopy at varying temperatures for phases of the $Li_{2+x}S_{1-x}N_x$ solid solution (i.e. x=0.05, 0.1, 0.2, 0.25, 0.45) (b) Percolation-energy diagram for different phases in the $Li_{2+x}S_{1-x}N_x$ solid-solution. (c) Correlation between the energy of percolation onset and the activation energies from impedance spectroscopy experiments.

340   We further calculated the corresponding percolation-energy diagrams for the $Li_{2+x}S_{1-x}N_x$ (x=0.05,

341   0.1, 0.2 0.25, 0.45) phases (Figure 7b) which show increasingly lower energies of percolation

342   onset demonstrating that indeed higher nitrogen content enables diffusion at lower energy

343   thresholds. Taken together with the experimental conductivity results, we arrive at a coherent

19

344 picture of how nitrogen content in the disordered $Li_{2+x}S_{1-x}N_x$ (0<x<0.55) solution, modulates

345 lithium-ion diffusion by controlling the energy and distribution of local transition states.

346 Figure 7c highlights the correlation between low-energy percolation onsets and the ability of

347 phases to feature diffusion at low-energy thresholds which is reflected in low experimental

348 conductivity-activation energies. This correlation between the atomistic (Å/nm) simulation

349 results and the macroscopic (mm) experimental results underlines the applicability of the

350 MD-percolation approach to rationalize property-composition relationships in disordered

351 systems.

352 In conclusion, we demonstrate here a previously unknown partial solid solution in the

353 $(1-x)Li_2S-xLi_3N$ tieline, spanning 0<x<0.55, accessible only by mechanochemistry and crystallizing

354 in antifluorite-like $Fm\overline{3}m$. The increasing conductivity with increasing nitrogen content in

355 antifluorite-like $Li_{2+x}S_{1-x}N_x$ (0<x<0.55) phases can be rationalized by the increased number of low-

356 energy N-rich bottlenecks enabling more percolating lithium-diffusion paths with lower energy

357 thresholds.

Perspectives for disordered, fully-reduced antifluorite solid electrolytes

359 Solid electrolytes should feature high ionic conductivity and (electro-)chemical stability against

360 both electrodes. The $Li_{2+x}S_{1-x}N_x$ phases presented here reach ~0.2 mS cm^{-1} and further

361 improvements of the ionic conductivity may be achieved by further compositional modifications

362 which are very likely possible based on reports nitride-chloride[16,34,35] and phosphide-sulfide[18]

363 phases with similar antifluorite-like structures, suggesting a large chemical space remaining to be

364 investigated. The $Li_{2+x}S_{1-x}N_x$ phases are structurally analogous to the recently discovered $Li_{2+x}S_{1-x}P_x$

365 phases which highlights the possibility to substitute phosphide P^{3-} anions (r≈1.89 Å, Table S5) by

366 significantly smaller N^{3-} anions (r≈1.46 Å, Table S5). For a given pnictide content (x) the $Li_{2+x}S_{1-x}N_x$

367 phases feature higher conductivities than the $Li_{2+x}S_{1-x}P_x$ phases (see SI Figure S10) possibly

368 because the smaller N^{3-} radii increases the bottleneck diameter.

369 Regarding (electro-)chemical stability against electrodes, due to their irreducible nature

370 $Li_{2+x}S_{1-x}N_x$ phases are thermodynamically stable at low potentials down to 0 V vs Li/Li$^+$ (see also

20

371 Supplementary Note 11) and thus intrinsically inert to reduction in contact with low-voltage next-

372 generation anodes such as lithium metal or silicon. Indeed we demonstrate in Figure 8a stable

373 lithium stripping/deposition in Li/Li$_{2.55}$S$_{0.45}$N$_{0.55}$/Li cells over hundreds of hours.

374 While irreducible, based on our preliminary linear-sweep voltammetry experiments shown in SI

375 Figure S11 the Li$_{2+x}$S$_{1-x}$N$_x$ phases can be oxidized at modest voltages. For low nitrogen content the

376 anodic limit lies close to 2 V (vs Li/Li$^+$) which is close to the anodic limit of Li$_2$S. With increasing

377 nitrogen content, while the ionic conductivity increases, the anodic limit decreases to ~1.25 V

378 (for x=0.45). These low anodic limits are still significantly higher than the anodic limit of Li$_3$N of

379 ca. 0.8 V vs Li/Li$^+$ (SI Figure S11). While equally inert to reductive decomposition, the increased

380 oxidative stability may be a key advantage of antifluorite-like Li$_{2+x}$S$_{1-x}$N$_x$ (0<x<0.55) phases over

381 Li$_3$N to enable next-generation anodes.

382 For example, considering that the operation window of Li$_x$Si anodes ranges from 0.01 V to 1.1 V,

383 Li$_3$N would oxidize against Li$_x$Si anodes due to its low anodic limit of ~0.8 V vs Li (Figure 8c). In

384 contrast, antifluorite-like Li$_{2+x}$S$_{1-x}$N$_x$ phases would be more suitable protection layers against Li$_x$Si

385 anodes as they would be inert to reduction **and** oxidation against Li$_x$Si anodes. We thus envisage

386 that Li$_{2+x}$S$_{1-x}$N$_x$ and related irreducible electrolytes could be applied as anolytes or protective

387 layers against low-potential anodes, in conjunction with a catholyte. As a proof of concept, we

388 demonstrate in Figure 8b and in Supplementary Note 11 that Li$_{2+x}$S$_{1-x}$N$_x$ (0<x<0.55) phases may

389 be used to prevent catastrophic decomposition of the Li$_2$ZrCl$_6$ solid electrolyte against lithium

390 metal electrodes. These examples demonstrate that inertness to reduction is not the sole

391 suitability criterion of anolytes and highlights the potential of new highly conducting irreducible

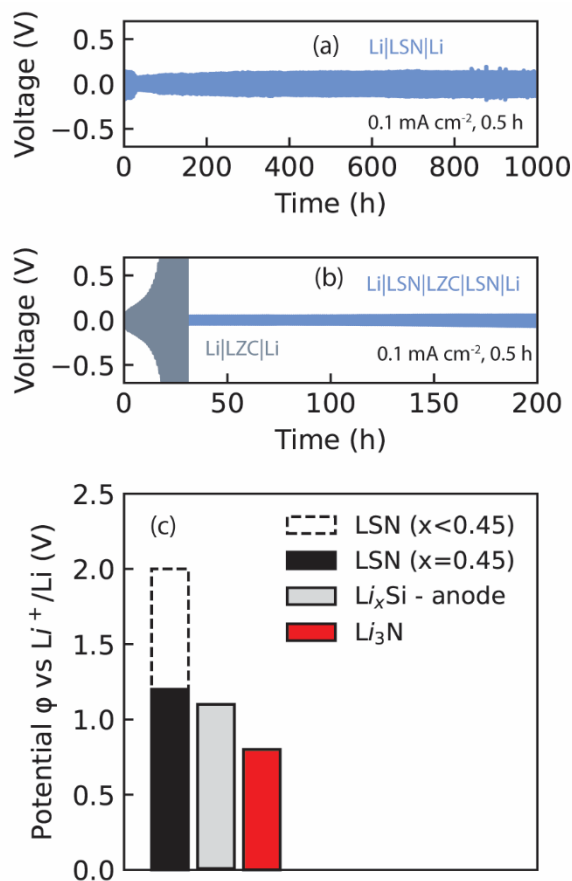392 phases for enabling next-generation solid-state batteries.

21

Figure 8. Electrochemical characterization of $Li_{2+x}S_{1-x}N_x$ (0<x<0.55) phases. (a) Symmetric $Li/Li_{2.45}S_{0.45}N_{0.55}/Li$ cell cycled at 0.1 mA cm^{-2}, 0.5 h of plating and stripping. (b) Symmetric $Li/Li_{2.45}S_{0.45}N_{0.55}/Li_2ZrCl_6/Li_{2.45}S_{0.45}N_{0.55}/Li$ and symmetric $Li/Li_2ZrCl_6/Li$ cells. Catastrophic voltage increase of $Li/Li_2ZrCl_6/Li$ cells is inhibited by protection against Li-metal with a $Li_{2+x}S_{1-x}N_x$ phase. (c) Black: Stability window of the of $Li_{2+x}S_{1-x}N_x$ phases, increasing with nitrogen content. Red: Stability window of Li_3N. Grey: Potential window over which Li_xSi (*silicon*) anodes operate.

Conclusion

In this study we report the discovery of a new family of irreducible solid electrolytes by dissolving lithium nitride into the antifluorite Li_2S resulting in crystalline $Li_{2+x}S_{1-x}N_x$ (0<x<0.55) lithium-rich antifluorite phases reaching high conductivities >0.2 mS cm^{-1} at room temperature. Leveraging a thorough diffusion-percolation analysis, we develop a widely applicable analysis approach and clarify the mechanism by which compositional disorder unlocks high conductivities in these solid electrolytes.

22

400 Using the examples of ordered and disordered-Li_9S_3N we demonstrate how the rich diversity of

401 coordination-environment compositions creates new lithium sites and bottlenecks, enabling low-

402 energy-percolating diffusion pathways. In particular, we identify the composition of the

403 bottlenecks as highly correlated with the local jump-activation energy, with nitride-rich

404 bottlenecks favoring diffusion. Based on this observation we endeavor to maximize nitrogen

405 content, in the process discovering a solid solution of $Li_{2+x}S_{1-x}N_x$ (0<x<0.55) antifluorite

406 electrolytes reaching 0.2 mScm^{-1} for the maximum nitrogen composition of $Li_{2.55}S_{0.45}N_{0.55}$.

407 Based on our combined experimental(EIS)-computational(AIMD-percolation) analyses on

408 $Li_{2+x}S_{1-x}N_x$ we establish that nitrogen-richer compositions indeed show higher conductivities and

409 lower conductivity-activation energies that can be rationalized by lower percolation onset

410 energies due to the increased occurrence of low jump-activation energy, nitrogen-rich

411 bottlenecks.

412 The new $Li_{2+x}S_{1-x}N_x$ (0<x<0.55) electrolytes we discovered are irreducible, thus

413 thermodynamically stable against all known next-generation low-potential anode materials for

414 batteries. Their high conductivities and stability at low potentials make these new electrolytes a

415 natural choice for much needed anolytes and protection layers combination with low-potential,

416 high-capacity anodes such as Si or Li metal.

417 Most relevantly, our results shed light on the mechanism by which structural disorder can affect

418 ionic conductivity in solids. Contrary to recent research trends, we show that high compositional

419 complexity (e.g. in so called *high-entropy* materials) is not necessary to access the disorder-

420 mediated improvements of ionic conductivity. Instead, by comparing disordered Li_9S_3N and

421 Li_6PS_5Br argyrodite to their ordered counterparts of the same composition, we demonstrate that

422 stabilizing metastable configurations of compositionally simple (*low entropy*) materials —e.g.

423 through mechanochemistry, quenching or soft-chemical approaches— can be sufficient to effect

424 dramatic ionic conductivity improvements without invoking compositional complexity.

Methodology

426 **Synthesis.** *$Li_{2+x}S_{1-x}N_x$ phases:* The synthesis precursors were Li_2S (Sigma-Aldrich, 99%) and Li_3N

427 (Sigma-Aldrich, >99.5%). Stoichiometric amounts of the precursors were milled in a planetary ball

428   mill (Jar: ZrO_2 , 45 mL) with 10 mm ZrO_2 balls and a ball:powder mass ratio of 30 at 550 rpm for

429   99 (5-min milling-5 min-pause) cycles. *Ordered*-Li_9S_3N**:** We closely followed the procedure

430   described by Miara and coworkers[22]. A planetary ball mill jar with 10 mm ZrO_2 balls and a

431   ball/powder ratio of 30 at 550 rpm for 99 (5-min-milling-5 min-pause) cycles was used to mix the

432   precursors Li_2S and Li_3N. Subsequently the powder mixture was transferred to tungsten crucibles

433   and sealed into quartz glass ampoules under 200 mbar of argon. The ampoules were then heated

434   (100°C/h) to 600 °C held at this temperature for 24 h and then slowly (over the course of 24 h)

435   cooled down to RT. All preparation steps were performed in an argon atmosphere ($H_2O < 1$ ppm,

436    $O_2 < 1$ ppm).

437   **Electrochemical Characterization.** *Electrochemical Impedance Spectroscopy (EIS):* Pellets

438   (diameter=10 mm) of the $Li_{2+x}S_{1-x}N_x$ probes were pressed (3.2 tons) in custom-made solid-state

439   lab cells. These lab cells consist of an alumina tube and two stainless steel plungers. Solid

440   electrolyte powder is filled in the alumina tube and compressed on both sides with the stainless

441   steel plungers. The cell configuration used was SS| $Li_{2+x}S_{1-x}N_x$ |SS (SS=stainless steel). AC

442   impedance was performed with a Metrohm Autolab (AUT86298) in the frequency range 10 MHz

443   to 0.1 Hz with a voltage amplitude of 10 mV. *Linear sweep voltammetry (LSV):* LSV measurements

444   were also performed with an Metrohm Autolab (AUT86298). To measure the anodic limit of

445    $Li_{2+x}S_{1-x}N_x$ phases, Li| $Li_{2+x}S_{1-x}N_x$ | $Li_{2+x}S_{1-x}N_x$ -C cells were used. To make the $Li_{2+x}S_{1-x}N_x$ -C

446   composite cathode a mixture of $Li_{2+x}S_{1-x}N_x$:Super P with a weight ratio of 0.7:0.3 was milled in a

447   planetary ball mill (Jar: ZrO_2 , 45 mL) with 10 mm ZrO_2 balls and a ball/powder ratio of 30 at 400

448   rpm for 2 h (5 min milling; 5 min pause). Li| $Li_{2+x}S_{1-x}N_x$ | $Li_{2+x}S_{1-x}N_x$ -C cells were assembled by

449   pressing a $Li_{2+x}S_{1-x}N_x$ pellet (130 mg, 3.2 tons) and subsequently the $Li_{2+x}S_{1-x}N_x$ -C composite (15

450   mg, 3.2 tons) on top of it. Finally, a Li disk was placed on the opposite side of the $Li_{2+x}S_{1-x}N_x$ pellet.

451   The LSV scanning rate was 0.01 mV s^{-1}. *Conductivity measurements at different temperatures for*

452   *Arrhenius fits:* SS| $Li_{2+x}S_{1-x}N_x$ |SS cells were kept at 30°C for 1h, then heated in 5 min to 50°C and

453   kept at this temperature for 30 min followed by heating to 60°C in 5 min and maintaining the

454   temperature for 30 min. This procedure was continued up to 100°C. The EIS obtained at the end

455   of the 30 min temperature-plateaus were used for Arrhenius fits.

X-ray diffraction. Powder diffraction patterns were collected using Cu Kα X-rays (1.54 Å) on a PANalytical X'Pert Pro X-ray diffractometer in Bragg-Brenano (*reflection*) geometry up to a $2\theta_{max}\approx80°$ ($q_{max}\approx 5.2$ Å^{-1}). The air sensitive $Li_{2+x}S_{1-x}N_x$ probes were loaded into air-tight holders in an Ar-filled glovebox prior to the measurements. GSAS-II[36] and FullProf[37] (through the user interface implemented in the "Match!" software) were used for LeBail and Rietveld refinements.

Neutron diffraction. Neutron powder diffraction data were collected on the PEARL neutron powder diffractometer at the research reactor of TU Delft.[38] Approximately 4 g of samples were loaded on 6-mm diameter cylindrical vanadium holders and sealed using indium wire under Ar atmosphere. Measurements were collected of the powder samples at room temperature with a neutron wavelength of 1.667 Å selected using the 533 reflection of a Ge monochromator, in transmission geometry up to a $2\theta_{max}\approx155°$ ($q_{max}\approx 7.3$ Å^{-1}).

Computational details. All DFT calculations were performed with the Vienna ab-initio simulation package VASP with computational settings consistent with those used in the Materials Project database. [39] For the generation and analysis of supercells the calculations were done on 2x2x2 $Li_{2+x}S_{1-x}N_x$ supercells. Because of the shared site occupations and partial occupancies in $Li_{2+x}S_{1-x}N_x$ phases different atomic arrangements were generated by random decoration of the Wyckoff 4a (0,0,0) position with nitrogen and sulfur and the 4b (0.5,0.5,0.5) positions were randomly decorated with Li and vacancies. The Wyckoff 8c (0.25,0.25,0.25) position was fully occupied with Li for all stoichiometries. For the generation and analysis of supercells the pymatgen package was used.[40] For the AIMD simulations the Li pseudopotential was changed from Li_sv (which was used for relaxations) to Li as this enables the use of a lower energy cutoff. The simulation time was > 200 ps for every AIMD simulation. The AIMD simulations were executed at 900 K. The dissection of AIMD simulations into individual jump events and subsequent analysis of jump frequencies and individual $E_{a,\ Jump}$ values was done as first described by de Klerk and Wagemaker;[23] a comprehensive account can be found in ref [23] but crucial aspects for the understanding of the reported data is presented here: *Partitioning of the supercell volume into site and non-site voxels:* The lithium site centers are obtained from crystallography and the site radii are set to the average vibrational amplitude of the Li-ions as described in ref. [23], which amounts to ca. 0.44 Å for the present simulations. Given the site center and site radius, spherical sites are defined around the

25

485 site-center. *Calculation of $E_{a, jump}$ values between two sites:* The sites are defined around the 0 K

486 equilibrium positions of the Li ions. At every simulation step it is recorded in which site each Li

487 ion is located or whether it is currently between two sites. From this information the jump

488 frequency between two site $v_{A->B}$ can be calculated according to equation 3:

489
$$v_{A \rightarrow B} = \frac{N_{A \rightarrow B}}{\tau_A} \quad (3)$$

490 where $v_{A->B}$ is the jump frequency for jumps from site A to site B, $N_{A->B}$ is the number of recorded

491 jumps from A to B, and τ_A is the time of occupation of site A. $E_{a, jump}$ is then obtained from equation

492 (1). The uncertainty on the average jump-Ea value for a jump type can be obtained from the

493 standard deviation of the mean (ε_{mean}) and the uncertainty associated with convergence

494 ($\varepsilon_{convergence}$, as further detailed in Supplementary Note 6) so that the total uncertainty on average

495 jump-Ea values is $\varepsilon_{jump-ea} = \varepsilon_{mean} + \varepsilon_{convergence}$ and is typically on the range of 10-30 meV. This whole

496 analysis is strongly supported by the gemdat (ref [41]) python package currently developed in our

497 group.

498 *Percolation model*: We performed AIMD simulations on 8 selected supercells that in sum

499 contained all jump events present in the disordered $Li_{2+x}S_{1-x}N_x$ phases (incl. disordered-Li_9S_3N);

500 this enabled the construction of a *jump library* with an average jump-Ea value for each jump

501 event, shown in SI Tables S3 and S4. The jump events for ordered-Li_9S_3N were obtained from an

502 AIMD simulation of and ordered-Li_9S_3N supercell. Subsequently a percolation analysis could be

503 performed on 50 (5x5x5) supercells for each of the different $Li_{2+x}S_{1-x}N_x$ stoichiometries

504 (x=0.05,0.1, 0.2, 0.25,0.3, 0.4, 0.5, 0.6, 0.7, 0.8, 0.9). The percolation analysis works as follows:

505 An activation energy cutoff is defined. Two sites A and B are connected if a randomly picked

506 element in the range [jump-Ea$_{(A->B)}$ -uncertainty, jump-Ea$_{(A->B)}$+uncertainty] and a randomly

507 picked element in the range [jump-Ea$_{(B->A)}$ -uncertainty, jump-Ea$_{(B->A)}$+uncertainty] are below the

508 activation energy cutoff. In this way a graph can be constructed which we did using the rustworkX

509 package ref [42]. If a path extends throughout the supercell the path is considered percolating,

510 provided that the endpoint of the percolation path is equally a starting point of a percolating

511 path (see SI Figure S5). For a given supercell and a given energy cutoff the analysis needs to be

512 repeated until the average fraction of sites in the percolation network converges. In cases where

26

513   only a subset of supercells were percolating at a given cutoff the average fraction of percolating

514   sites was obtained from percolating supercells. The standard deviation of the distribution of

515   fractions at one cutoff energy was taken as the uncertainty on the fraction of active Li sites.

516   *Bottleneck size calculations:* 50 disordered Li_9S_3N supercells were relaxed (containing > 9000

517   bottlenecks) to account for local distortions which may not be present in long-range averaged

518   crystallographic unit cells. The three atoms at the vertices of triangular bottlenecks connecting

519   sites were identified and the inner-circle diameter using the sympy Triangle package. For the

520   calculation of bottleneck diameters the biangle line (line that "cuts an angle in half") was followed

521   by the distance of the ion-radius of the ion located at the vertex. This was done at all three

522   vertices so that a new triangle is formed. The outer-circle diameter of this new triangle is

523   determined by the sympy (ref [43]) Triangle package and is the bottleneck diameter. For each type

524   of bottleneck (i.e. NSS, NNS…) the average diameter is determined and the standard deviation

525   of the distribution of diameters is shown as the error bar.

Data Availability

527   The data that support the findings of this study and the code to reproduce the results shown in

528   the paper are openly available in 4TU.ResearchData at http://doi.org/10.4121/f3632023-c54e-

529   4c95-848b-3e4db819bbf7 . We used python version 3.10 and the following python packages:

530   numpy [44], gemdat [41], matplotlib [45], pymatgen [40], rustworkx [42], sympy [43]

531

Author Contributions

533   The study was conceptualized by V.L. Simulation data were acquired by V.L ($Li_{2-x}S_{1-x}N_x$), A.V. and

534   A.L. ($Li_{6-x}PS_{5-x}Br_{1+x}$). Experimental data were acquired by V.L, M.T., J.d.L., W.Z. and Z.C. (synthesis,

535   x-ray diffraction, electrochemistry), J.C. (x-ray photoelectron spectroscopy), T.F. (neutron

536   diffraction). Data analysis and interpretation were done by V.L., T.F , M.T. and M.W. Writing and

537   editing of the draft were done by V.L., T.F., M.W., A.V. and S.G. The funding for this study was

538   acquired by M.W and T.F. The work was supervised by T.F. and M.W. All authors have approved

539   the submitted version of the manuscript.

540

Acknowledgements

The following references are cited in the Supplementary Information refs. [6,21,47–56,25,57–66,27,28,30–33,46.

After the initial submission of this study [ref. 67] and during revisions for publication, an article on related subject matter has appeared [ref. 68] .

References

(1)   Janek, J.; Zeier, W. G. Challenges in Speeding up Solid-State Battery Development. *Nat. Energy* **2023**, *8* (3), 230–240.

(2)   Betz, J.; Bieker, G.; Meister, P.; Placke, T.; Winter, M.; Schmuch, R. Theoretical versus Practical Energy: A Plea for More Transparency in the Energy Calculation of Different Rechargeable Battery Systems. *Adv. energy Mater.* **2019**, *9* (6), 1803170.

(3)   Lewis, J. A.; Cavallaro, K. A.; Liu, Y.; McDowell, M. T. The Promise of Alloy Anodes for Solid-State Batteries. *Joule* **2022**, *6* (7), 1418–1430.

(4)   Janek, J.; Zeier, W. G. A Solid Future for Battery Development. *Nat. Energy* **2016**, *1* (9), 1–4.

(5)   Krauskopf, T.; Richter, F. H.; Zeier, W. G.; Janek, J. Physicochemical Concepts of the Lithium Metal Anode in Solid-State Batteries. *Chem. Rev.* **2020**, *120* (15), 7745–7794.

(6)   Zhu, Y.; He, X.; Mo, Y. First Principles Study on Electrochemical and Chemical Stability of Solid Electrolyte-Electrode Interfaces in All-Solid-State Li-Ion Batteries. *J. Mater. Chem. A* **2016**, *4* (9), 3253–3266.

(7)   Schwietert, T. K.; Arszelewska, V. A.; Wang, C.; Yu, C.; Vasileiadis, A.; de Klerk, N. J. J.; Hageman, J.; Hupfer, T.; Kerkamm, I.; Xu, Y. Clarifying the Relationship between Redox Activity and Electrochemical Stability in Solid Electrolytes. *Nat. Mater.* **2020**, *19* (4), 428–435.

(8)   Kim, K.; Park, D.; Jung, H.-G.; Chung, K. Y.; Shim, J. H.; Wood, B. C.; Yu, S. Material Design Strategy for Halide Solid Electrolytes Li_3MX_6 (X= Cl, Br, and I) for All-Solid-State High-Voltage Li-Ion Batteries. *Chem. Mater.* **2021**, *33* (10), 3669–3677.

(9)   Lohrberg, O.; Voigt, K.; Maletti, S.; Auer, H.; Nikolowski, K.; Heubner, C.; Michaelis, A. Benchmarking and Critical Design Considerations of Zero-Excess Li-Metal Batteries. *Adv. Funct. Mater.* **2023**, 2214891.

(10)   Han, F.; Zhu, Y.; He, X.; Mo, Y.; Wang, C. Electrochemical Stability of $Li_{10}GeP_2S_{12}$ and $Li_7La_3Zr_2O_{12}$ Solid Electrolytes. *Adv. Energy Mater.* **2016**, *6* (8), 1501590.

(11)   Huo, H.; Janek, J. Silicon as Emerging Anode in Solid-State Batteries. *ACS Energy Lett.* **2022**, *7* (11), 4005–4016.

579   (12)   Sun, Y.; Li, Y.; Sun, J.; Li, Y.; Pei, A.; Cui, Y. Stabilized Li3N for Efficient Battery Cathode

580   Prelithiation. *Energy Storage Mater.* **2017**, *6* (October 2016), 119–124.

581   (13)   Park, S. W.; Choi, H. J.; Yoo, Y.; Lim, H.; Park, J.; Lee, Y.; Ha, Y.; Lee, S.; Kim, B. G. Stable Cycling of

582   All-solid-state Batteries with Sacrificial Cathode and Lithium-free Indium Layer. *Adv. Funct.*

583   *Mater.* **2022**, *32* (5), 2108203.

584   (14)   Zheng, J.; Perry, B.; Wu, Y. Antiperovskite Superionic Conductors: A Critical Review. *ACS Mater.*

585   *Au* **2021**, *1* (2), 92–106.

586   (15)   Dawson, J. A.; Famprikis, T.; Johnston, K. E. Anti-Perovskites for Solid-State Batteries: Recent

587   Developments, Current Challenges and Future Prospects. *J. Mater. Chem. A* **2021**, *9* (35), 18746–

588   18772.

589   (16)   Landgraf, V.; Famprikis, T.; de Leeuw, J.; Bannenberg, L. J.; Ganapathy, S.; Wagemaker, M. Li_5NCl_2

590   : A Fully-Reduced, Highly-Disordered Nitride-Halide Electrolyte for Solid-State Batteries with

591   Lithium-Metal Anodes. *ACS Appl. Energy Mater.* **2023**, *6* (3), 1661–1672.

592   (17)   Li, W.; Li, M.; Chien, P.; Wang, S.; Yu, C.; King, G.; Hu, Y.; Xiao, Q.; Shakouri, M.; Feng, R.; Fu, B.;

593   Abdolvand, H.; Fraser, A.; Li, R.; Huang, Y.; Liu, J.; Mo, Y.; Sham, T.; Sun, X. Lithium-Compatible

594   and Air-Stable Vacancy-Rich $Li_9N_2Cl_3$ for High – Areal Capacity , Long-Cycling All – Solid-State

595   Lithium Metal Batteries. **2023**.

596   (18)   Szczuka, C.; Karasulu, B.; Groh, M. F.; Sayed, F. N.; Sherman, T. J.; Bocarsly, J. D.; Vema, S.;

597   Menkin, S.; Emge, S. P.; Morris, A. J.; Grey, C. P. Forced Disorder in the Solid Solution $Li_3P–Li_2S$: A

598   New Class of Fully Reduced Solid Electrolytes for Lithium Metal Anodes. *J. Am. Chem. Soc.* **2022**,

599   *144* (36), 16350–16365.

600   (19)   Xu, X.; Du, G.; Cui, C.; Liang, J.; Zeng, C.; Wang, S.; Ma, Y.; Li, H. Stabilizing the Halide Solid

601   Electrolyte to Lithium by a β-Li_3N Interfacial Layer. *ACS Appl. Mater. Interfaces* **2022**, *14* (35),

602   39951–39958.

603   (20)   Zeng, Y.; Ouyang, B.; Liu, J.; Byeon, Y. W.; Cai, Z.; Miara, L. J.; Wang, Y.; Ceder, G. High-Entropy

604   Mechanism to Boost Ionic Conductivity. *Science (80-.).* **2022**, *378* (6626), 1320–1324.

605   (21)   Marx, R.; Lissner, F.; Schleid, T. $Li_9N_2S_3$: Das Erste Nitridsulfid Der Alkalimetalle in Einer Li2O-Typ-

606   Variante. *Zeitschrift für Anorg. und Allg. Chemie* **2006**, *632* (12-13), 2151.

30

607　(22)　Miara, L. J.; Suzuki, N.; Richards, W. D.; Wang, Y.; Kim, J. C.; Ceder, G. Li-Ion Conductivity in Li_9S_3N.
608　　　　　*J. Mater. Chem. A* **2015**, *3* (40), 20338–20344.

609　(23)　De Klerk, N. J. J.; Van Der Maas, E.; Wagemaker, M. Analysis of Diffusion in Solid-State
610　　　　　Electrolytes through MD Simulations, Improvement of the Li-Ion Conductivity in β-Li_3PS_4 as an
611　　　　　Example. *ACS Appl. Energy Mater.* **2018**, *1* (7), 3230–3242.

612　(24)　Yu, C.; Ganapathy, S.; De Klerk, N. J. J.; Roslon, I.; Van Eck, E. R. H.; Kentgens, A. P. M.;
613　　　　　Wagemaker, M. Unravelling Li-Ion Transport from Picoseconds to Seconds: Bulk versus Interfaces
614　　　　　in an Argyrodite Li_6PS_5Cl-Li_2S All-Solid-State Li-Ion Battery. *J. Am. Chem. Soc.* **2016**, *138* (35),
615　　　　　11192–11201.

616　(25)　De Klerk, N. J. J.; Rosłoń, I.; Wagemaker, M. Diffusion Mechanism of Li Argyrodite Solid
617　　　　　Electrolytes for Li-Ion Batteries and Prediction of Optimized Halogen Doping: The Effect of Li
618　　　　　Vacancies, Halogens, and Halogen Disorder. *Chem. Mater.* **2016**, *28* (21), 7955–7963.

619　(26)　De Klerk, N. J. J.; Wagemaker, M. Diffusion Mechanism of the Sodium-Ion Solid Electrolyte Na_3PS_4
620　　　　　and Potential Improvements of Halogen Doping. *Chem. Mater.* **2016**, *28* (9), 3122–3130.

621　(27)　Morgan, B. J. Mechanistic Origin of Superionic Lithium Diffusion in Anion-Disordered Li6PS5X
622　　　　　Argyrodites. *Chem. Mater.* **2021**, *33* (6), 2004–2018.

623　(28)　He, X.; Zhu, Y.; Mo, Y. Origin of Fast Ion Diffusion in Super-Ionic Conductors. *Nat. Commun.* **2017**,
624　　　　　*8* (May), 1–7.

625　(29)　Van der Ven, A.; Ceder, G.; Asta, M.; Tepesch, P. D. First-Principles Theory of Ionic Diffusion with
626　　　　　Nondilute Carriers. *Phys. Rev. B* **2001**, *64* (18), 184307.

627　(30)　Almond, D. P.; Duncan, G. K.; West, A. R. The Determination of Hopping Rates and Carrier
628　　　　　Concentrations in Ionic Conductors by a New Analysis of Ac Conductivity. *Solid State Ionics* **1983**,
629　　　　　*8* (2), 159–164.

630　(31)　Wang, Z.; Mishra, T. P.; Xie, W.; Deng, Z.; Gautam, G. S.; Cheetham, A. K.; Canepa, P. Kinetic
631　　　　　Monte Carlo Simulations of Sodium Ion Transport in NaSICON Electrodes. *ACS Mater. Lett.* **2023**,
632　　　　　*5* (9), 2499–2507.

633　(32)　Deng, Z.; Mishra, T. P.; Mahayoni, E.; Ma, Q.; Tieu, A. J. K.; Guillon, O.; Chotard, J.-N.; Seznec, V.;
634　　　　　Cheetham, A. K.; Masquelier, C. Fundamental Investigations on the Sodium-Ion Transport

31

635   Properties of Mixed Polyanion Solid-State Battery Electrolytes. *Nat. Commun.* **2022**, *13* (1), 4470.

636   (33)   Shannon, R. D. Revised Effective Ionic Radii and Systematic Studies of Interatomic Distances in

637   Halides and Chalcogenides. *Acta Crystallogr. Sect. A Cryst. physics, diffraction, Theor. Gen.*

638   *Crystallogr.* **1976**, *32* (5), 751–767.

639   (34)   Li, W.; Li, M.; Chien, P.-H.; Wang, S.; Yu, C.; King, G.; Hu, Y.; Xiao, Q.; Shakouri, M.; Feng, R.

640   Lithium-Compatible and Air-Stable Vacancy-Rich Li9N2Cl3 for High–Areal Capacity, Long-Cycling

641   All–Solid-State Lithium Metal Batteries. *Sci. Adv.* **2023**, *9* (42), eadh4626.

642   (35)   Marx, R.; Mayer, H. M. Preparation and Crystal Structure of Ordered and Disordered Lithium

643   Nitride Dichloride, Li5NCl2. *J. Solid State Chem.* **1997**, *130* (1), 90–96.

644   (36)   Toby, B. H.; Von Dreele, R. B. GSAS-II: The Genesis of a Modern Open-Source All Purpose

645   Crystallography Software Package. *J. Appl. Crystallogr.* **2013**, *46* (2), 544–549.

646   (37)   Rodriguez-Carvajal, J. In Satellite Meeting on Powder Diffraction of the XV Congress of the IUCr,

647   1990, 127. *Toulouse, Fr.*

648   (38)   Van Eijck, L.; Cussen, L. D.; Sykora, G. J.; Schooneveld, E. M.; Rhodes, N. J.; Van Well, A. A.;

649   Pappas, C. Design and Performance of a Novel Neutron Powder Diffractometer: PEARL at TU

650   Delft. *J. Appl. Crystallogr.* **2016**, *49* (5), 1398–1401.

651   (39)   Jain, A.; Ong, S. P.; Hautier, G.; Chen, W.; Richards, W. D.; Dacek, S.; Cholia, S.; Gunter, D.;

652   Skinner, D.; Ceder, G.; Persson, K. A. Commentary: The Materials Project: A Materials Genome

653   Approach to Accelerating Materials Innovation. *APL Mater.* **2013**, *1* (1), 001002.

654   (40)   Ong, S. P.; Richards, W. D.; Jain, A.; Hautier, G.; Kocher, M.; Cholia, S.; Gunter, D.; Chevrier, V. L.;

655   Persson, K. A.; Ceder, G. Python Materials Genomics (Pymatgen): A Robust, Open-Source Python

656   Library for Materials Analysis. *Comput. Mater. Sci.* **2013**, *68*, 314–319.

657   (41)   Azizi, V.; Smeets, S.; Lavrinenko, A. K.; Ciarella, S.; Famprikis, T. GEMDAT. Zenodo July 2024.

658   (42)   Treinish, M.; Carvalho, I.; Tsilimigkounakis, G.; Sá, N. Rustworkx: A High-Performance Graph

659   Library for Python. *arXiv Prepr. arXiv2110.15221* **2021**.

660   (43)   Meurer, A.; Smith, C. P.; Paprocki, M.; Čertík, O.; Kirpichev, S. B.; Rocklin, M.; Kumar, Am.; Ivanov,

661   S.; Moore, J. K.; Singh, S. SymPy: Symbolic Computing in Python. *PeerJ Comput. Sci.* **2017**, *3*, e103.

662 (44) Harris, C. R.; Millman, K. J.; Van Der Walt, S. J.; Gommers, R.; Virtanen, P.; Cournapeau, D.;
663   Wieser, E.; Taylor, J.; Berg, S.; Smith, N. J. Array Programming with NumPy. *Nature* **2020**, *585*
664   (7825), 357–362.

665 (45) Hunter, J. D. Matplotlib: A 2D Graphics Environment. *Comput. Sci. \& Eng.* **2007**, *9* (3), 90–95.

666 (46) Conrad Szczuka; Bora Karasulu; Matthias F. Groh; Svetlana Menkin; Steffen P. Emge; Farheen N.
667   Sayed; Andrew J. Morris; Clare P. Grey. Forced Disorder in the Solid Solution Li3P–Li2S: A New
668   Class of Fully Reduced Solid Electrolytes for Lithium Metal Anodes, (Manuscript Submitted).
669   **2022**.

670 (47) Dong, Y.; DiSalvo, F. J. Reinvestigation of Trilithium Phosphide, Li3P. *Acta Crystallogr. Sect. E*
671   *Struct. Reports Online* **2007**, *63* (4), i97–i98.

672 (48) Van der Ven, A.; Ceder, G.; Asta, M.; Tepesch, P. D. First-Principles Theory of Ionic Diffusion with
673   Nondilute Carriers. *Phys. Rev. B - Condens. Matter Mater. Phys.* **2001**, *64* (18), 1–17.

674 (49) Catlow, C. R. A. STATIC LATTICE SIMULATION OF STRUCTURE AND TRANSPORT IN SUPERIONIC
675   CONDUCTORS. *Solid State Ionics* **1983**, *8* (SUPPL. 3), 89–107.

676 (50) Gautam, A.; Sadowski, M.; Ghidiu, M.; Minafra, N.; Senyshyn, A.; Albe, K.; Zeier, W. G.
677   Engineering the Site-Disorder and Lithium Distribution in the Lithium Superionic Argyrodite
678   Li6PS5Br. *Adv. Energy Mater.* **2021**, *11* (5).

679 (51) Zhao, E.; He, L.; Zhang, Z.; Doux, J.-M.; Tan, D. H. S.; Wu, E. A.; Deysher, G.; Chen, Y.-T.; Zhao, J.;
680   Wang, F. New Insights into Li Distribution in the Superionic Argyrodite Li 6 PS 5 Cl. *Chem.*
681   *Commun.* **2021**, *57* (82), 10787–10790.

682 (52) Zhou, L.; Minafra, N.; Zeier, W. G.; Nazar, L. F. Innovative Approaches to Li-Argyrodite Solid
683   Electrolytes for All-Solid-State Lithium Batteries. *Acc. Chem. Res.* **2021**, *54* (12), 2717–2728.

684 (53) Zhou, L.; Zhang, Q.; Nazar, L. F. Li-Rich and Halide-Deficient Argyrodite Fast Ion Conductors.
685   *Chem. Mater.* **2022**, *34* (21), 9634–9643.

686 (54) Hogrefe, K.; Minafra, N.; Hanghofer, I.; Banik, A.; Zeier, W. G.; Wilkening, H. M. R. Opening
687   Diffusion Pathways through Site Disorder: The Interplay of Local Structure and Ion Dynamics in
688   the Solid Electrolyte Li6+ x P1–x Ge x S5I as Probed by Neutron Diffraction and NMR. *J. Am.*
689   *Chem. Soc.* **2022**, *144* (4), 1795–1812.

33

690   (55)   Gautam, A.; Al-Kutubi, H.; Famprikis, T.; Ganapathy, S.; Wagemaker, M. Exploring the
691   Relationship Between Halide Substitution, Structural Disorder, and Lithium Distribution in
692   Lithium Argyrodites (Li6–x PS5–x Br1+ X). *Chem. Mater.* **2023**, *35* (19), 8081–8091.

693   (56)   Perdew, J. P.; Burke, K.; Ernzerhof, M. Generalized Gradient Approximation Made Simple. *Phys.*
694   *Rev. Lett.* **1996**, *77* (18), 3865.

695   (57)   Kresse, G.; Furthmüller, J. Efficiency of Ab-Initio Total Energy Calculations for Metals and
696   Semiconductors Using a Plane-Wave Basis Set. *Comput. Mater. Sci.* **1996**, *6* (1), 15–50.

697   (58)   Blöchl, P. E. Projector Augmented-Wave Method. *Phys. Rev. B* **1994**, *50* (24), 17953.

698   (59)   Nosé, S. A Unified Formulation of the Constant Temperature Molecular Dynamics Methods. *J.*
699   *Chem. Phys.* **1984**, *81* (1), 511–519.

700   (60)   Hoover, W. G. Canonical Dynamics: Equilibrium Phase-Space Distributions. *Phys. Rev. A* **1985**, *31*
701   (3), 1695.

702   (61)   Tilley, R. J. D. *Defects in Solids*; John Wiley & Sons, 2008.

703   (62)   Wert, C.; Zener, C. Interstitial Atomic Diffusion Coefficients. *Phys. Rev.* **1949**, *76* (8), 1169–1175.

704   (63)   Dienes, G. J. Frequency Factor and Activation Energy for the Volume Diffusion of Metals. *J. Appl.*
705   *Phys.* **1950**, *21* (11), 1189–1192.

706   (64)   Almond, D. P.; West, A. R. The Activation Entropy for Transport in Ionic Conductors. *Solid State*
707   *Ionics* **1987**, *23* (1–2), 27–35.

708   (65)   Gao, Y.; Li, N.; Wu, Y.; Yang, W.; Bo, S. H. Rethinking the Design of Ionic Conductors Using Meyer–
709   Neldel–Conductivity Plot. *Adv. Energy Mater.* **2021**, *11* (13), 1–9.

710   (66)   Du, P.; Zhu, H.; Braun, A.; Yelon, A.; Chen, Q. Entropy and Isokinetic Temperature in Fast Ion
711   Transport. *Adv. Sci.* **2024**, *11* (2), 1–8.

712   (67)   Landgraf, V.; Tu, M.; Cheng, Z.; de Leeuw, J.; Ganapathy, S.; Wagemaker, M.; Famprikis, T.
713   Entropy-Induced High Conductivity in Fully-Reduced Electrolytes for Solid-State Batteries with
714   Lithium Metal Anodes. *ChemRxiv* **2023**.

715   (68)   Yu, P.; Zhang, H.; Hussain, F.; Luo, J.; Tang, W.; Lei, J.; Gao, L.; Butenko, D.; Wang, C.; Zhu, J.; Yin,
716   W.; Zhang, H.; Han, S.; Zou, R.; Chen, W.; Zhao, Y.; Xia, W.; Sun, X. Lithium Metal-Compatible

34

717   Antifluorite Electrolytes for Solid-State Batteries. *J. Am. Chem. Soc.* **2024**.

718   (69)   Ji, H.; Urban, A.; Kitchaev, D. A.; Kwon, D. H.; Artrith, N.; Ophus, C.; Huang, W.; Cai, Z.; Shi, T.; Kim,

719   J. C.; Kim, H.; Ceder, G. Hidden Structural and Chemical Order Controls Lithium Transport in

720   Cation-Disordered Oxides for Rechargeable Batteries. *Nat. Commun.* **2019**, *10* (1).

721